Advances in Aircraft and Spacecraft Science, *Vol. 6, No. 6 (2019) 529-550*
DOI: https://doi.org/10.12989/aas.2019.6.6.529

Assessment of statistical sampling methods and approximation models applied to aeroacoustic and vibroacoustic problems

Till M. Biedermann*[1], Marius Reich[2a], Frank Kameier[1b], Mario Adam[2c] and C. O. Paschereit[3d]

[1]*Institute of Sound and Vibration Engineering ISAVE, University of Applied Sciences Duesseldorf, Muensterstrasse 156, D-40476 Dusseldorf, Germany*
[2]*Centre of Innovative Energy Systems ZIES, University of Applied Sciences Duesseldorf, Muensterstrasse 156, D-40476 Dusseldorf, Germany*
[3]*Institute of Fluid Dynamics and Technical Acoustics ISTA, Technical University Berlin, Mueller-Breslau-Strasse 8, D-10623, Berlin, Germany*

(Received September 5, 2018, Revised December 17, 2018, Accepted January 28, 2019)

Abstract. The effect of multiple process parameters on a set of continuous response variables is, especially in experimental designs, difficult and intricate to determine. Due to the complexity in aeroacoustic and vibroacoustic studies, the often-performed simple one-factor-at-a-time method turns out to be the least effective approach. In contrast, the statistical Design of Experiments is a technique used with the objective to maximize the obtained information while keeping the experimental effort at a minimum. The presented work aims at giving insights on Design of Experiments applied to aeroacoustic and vibroacoustic problems while comparing different experimental designs and approximation models. For this purpose, an experimental rig of a ducted low-pressure fan is developed that allows gathering data of both, aerodynamic and aeroacoustic nature while analysing three independent process parameters. The experimental designs used to sample the design space are a Central Composite design and a Box-Behnken design, both used to model a response surface regression, and Latin Hypercube sampling to model an Artificial Neural network. The results indicate that Latin Hypercube sampling extracts information that is more diverse and, in combination with an Artificial Neural network, outperforms the quadratic response surface regressions. It is shown that the Latin Hypercube sampling, initially developed for computer-aided experiments, can also be used as an experimental design. To further increase the benefit of the presented approach, spectral information of every experimental test point is extracted and Artificial Neural networks are chosen for modelling the spectral information since they show to be the most universal approximators.

Keywords: artificial neural networks, design of experiments; Latin hypercube sampling; aeroacoustics, aerodynamics, spectral analysis

*Corresponding author, Ph.D. Student, E-mail: till.biedermann@hs-duesseldorf.de
[a]Research Assistant, E-mail: marius.reich@hs-duesseldorf.de
[b] Professor, E-mail: frank.kameier@hs-duesseldorf.de
[c] Professor, E-mail: mario.adam@hs-duesseldorf.de
[d]Professor, E-mail: oliver.paschereit@tu-berlin.de

http://www.techno-press.org/?journal=aas&subpage=7 ISSN: 2287-528X (Print), 2287-5271 (Online)

1. Introduction

The acoustic signature of axial fans and blowers is known to be highly affected by the specific inflow conditions (Zenger *et al.* 2016, Amiet 1977, Daroukh *et al.* 2017). At smooth inflow conditions, the acoustic signature of a fan is mainly limited to noise radiation from the rotor trailing edges, struts as well as rotor speed-dependent effects like the blade passing frequency and rotor stator interaction. At given inflow condition of elevated turbulence intensity, however, a significant portion of leading edge noise of broadband character is added. This tends to dominate the acoustic signature of a fan in the low-to-intermediate frequency region, plus the occurrence of possible additional effects within the rotor, as for example the altering of flow separation phenomena. Recent research focussed on the establishment and evaluation of passive noise reduction mechanisms to significantly reduce the turbulence-induced leading edge noise (Biedermann *et al.* 2018, Biedermann *et al.* 2017).

As it is a commonly reported problem in aeroacoustic optimisation, opposing trends arise for the targets of low-noise-design while keeping the aerodynamic efficiency at a high level. Motivated by the described defiance, the question arose on how to best describe a multi-parameter system by taking into account target values of aerodynamic and aeroacoustic nature. Common statistical-empirical modelling approaches such as the Design of Experiments (DoE) methodology (Siebertz *et al.* 2010, Adam 2012) are limited to models of second order. These approaches are expected not to sufficiently describe systems of high complexity at the desired prediction accuracy, as is also concluded by this paper. Thus, these modelling approaches are compared to more advanced Artificial Neural networks (ANN), which are unlimited in terms of functional complexity and are generated by the use of a Latin Hypercube sampling. All three described approaches are used to model both, the aerodynamic and aeroacoustic performance of an axial fan by varying three continuous parameters, namely the fan speed, the throttling state as well as the level of incoming turbulence.

In recent research, experimental designs are adapted for numerical approaches (Alam *et al.* 2004) such as the Design of Experiments methodology. However, for the current analysis, the Latin Hypercube sampling (LHS) is applied to a complex problem of experimental character, even though it was initially designed for numerical machine learning processes (McKay *et al.* 1979, Reich *et al.* 2017). The results show that the artificial neural networks (ANN) based on the LHS are outperforming the more established Design of Experiments methods, in particular, when it comes to the highly non-linear target values of aeroacoustic and vibroacoustic nature. After identifying the ANNs in combination with the LHS as the most feasible approach to describe the experimental space with high accuracy, the next step inevitably leads towards a modelling of the not yet incorporated spectral composition of the aeroacoustic signals. Therefore, in a second step, the complex spectral information by means of the $1/3^{rd}$ octave bands are extracted for each measurement point of the data pool and are implemented in the current model to be approximated using Artificial Neural networks. The obtained additional networks provide deep insights into the spectral composition of the radiated noise, which might be essential for up-to-date low-noise design approaches.

2. Statistical approach

So-called experimental designs are commonly used for obtaining maximum information on a system while keeping the experimental effort at a minimum. A design consists of a different

combination of factor settings, so-called factor level combinations. However, the available approaches to sample the space of interest, which is defined by the maximum and minimum values of the parameters, show a large variety and must be defined prior to any experimental study.

For this study, three different experimental designs are used and compared by means of the number of necessary experiments and the resulting accuracy on evenly distributed test data. The first experimental design is the Circumscribed Central Composite design (C-CCD). The C-CCD consists of a two-level factorial design that samples information equidistantly on the inside of the design space as well as so-called star points that lie at the borders of the design space. Numerous centre points are sampled to establish predefined statistical properties, which are for this case orthogonality and rotatability. Orthogonality allows for a non-commingled estimation of factor effects in the successive modelling, while rotatability allows for the assumption that the variance of the predicted response is only a function of distance to the centre point. Consequently, the C-CCD consists of five different settings for each factor as can be seen in Fig. 1a, where the green rectangles represent the factorial design and the orange circles represent the star points. A compressed reading on Central Composite designs can be found in the engineering statistical handbook of NIST/SEMATECH (NIST/SEMATECH, 2003). The second experimental design is the Box Behnken design (BBD) (Box and Behnken 1960), which is a fractional three level design, exhibiting orthogonal statistical properties (see Fig. 1b and Appendix A). The BBD uses factor level combinations at the surfaces of the design space. Both, the C-CCD and the BBD, are used to model a quadratic response surface regression.

In contrast to the latter designs, the Latin Hypercube sampling (LHS) was developed for computer-aided experiments (McKay *et al.* 1979). One of its attributes is, that the number of settings for every factor (recall: three for BBD and five for C-CCD) equals the total number of factor level combinations (Fig. 1c and Appendix A). Consequently, every factor level combination is a unique setting. As a result, the LHS allows extracting more diverse information from the design space compared to the C-CCD and the BBD but leading to more cumbersome experiments, especially if a factor requires manufacturing effort. The creation of an LHS is of stochastic nature, which is the reason designs of more advantageous or disadvantageous nature can be created. To assess different designs, one or more criteria need to be used. For this case study, the MaxiMin criterion, evaluating the maximum-to-minimum Euclidean distance between the factor level combinations, and the pairwise correlation criterion, evaluating the order of commingled factors effects, are used to rate 15.000 randomly created designs. For further reading on LHS and possible optimisation criteria see for example (Viana 2013) or (Joseph and Hung 2016). To obtain additional information in the corners of the design space, a fractional two-level design is added to the LHS. The so created design can be seen in Fig. 1c and Appendix A. Instead of modelling a quadratic response surface regression, as if for the C-CCD and the BBD, the information sampled with the LHS are used to train an Artificial Neural network (ANN, for further details on ANNs see (Samarasinghe 2016)). To prevent the ANN from overfitting the data, it is split into samples for training (= adapting the parameters of the ANN) and validation (= assessing predictive capabilities on unused/ independent data).

To test the three generated models against independent data, ten additional measurements are conducted, where six measurements of this set cover uniformly distributed locations within the design space. The remaining four measurements, however, are located at the outer corners of the experimental space, which are traditionally hard to approximate by any model. This set of data serves, in addition to the models' coefficient of determination R^2, as quality characteristic for the single chosen approaches.

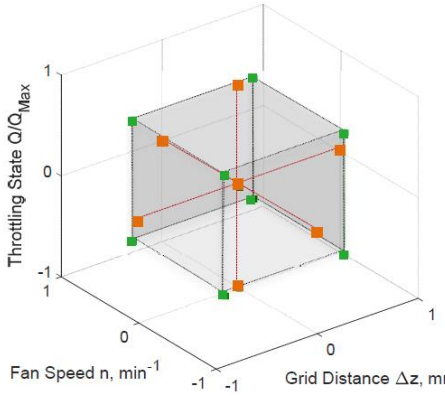

(a) Central Composite design C-CCD, 24 factor level combinations, orange circles = star points, green rectangles = full factorial two level design

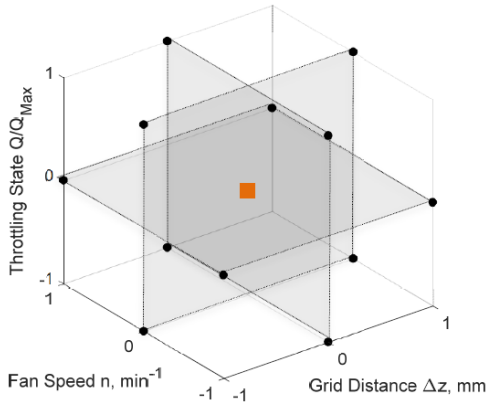

(b) Box Behnken design BBD, 15 factor level combinations, orange rectangle = central point

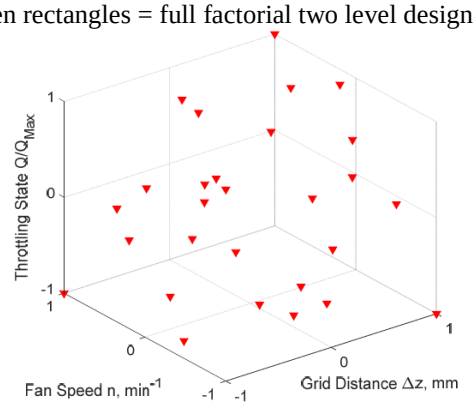

(c) Latin Hypercube sampling LHS, 28 unique factor level combinations

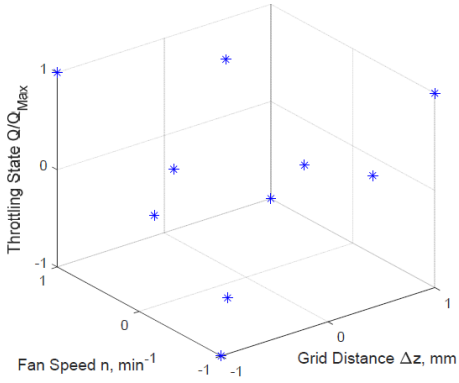

(d) Independent test samples, 10 unique factor level combinations

Fig. 1 Approaches to sample the experimental design space and additional test data for validation. All designs are presented in Appendix A in tabular form

3. Experimental setup

3.1 Test rig and rotor design

According to DIN ISO 5136 (ISO 5136) a test rig (Fig. 2), enabling the simultaneous measurement of the aerodynamic and aeroacoustic performance, is utilised to analyse a self-designed rotor, following the single aerofoil design technique (Carolus and Starzmann 2011). The rotor consists of six equidistantly distributed blades of C = 0.075 m chord and S = 0.1 m span where the blades follow the NACA65(12)-10 high-lift aerofoil profile (Fig. 3). Since a low complexity of the fan design is desired, no sweep, dihedral or shroud of the blades is applied to focus on the main aeroacoustic noise sources and to avoid possible masking and superimposing effects. The rotor is placed in a duct of D = 0.4 m in diameter, where the mounting takes place via eight struts downstream of the rotor, which itself are vibroacoustically decoupled from the duct to block the occurrence and propagation of solid-borne sound.

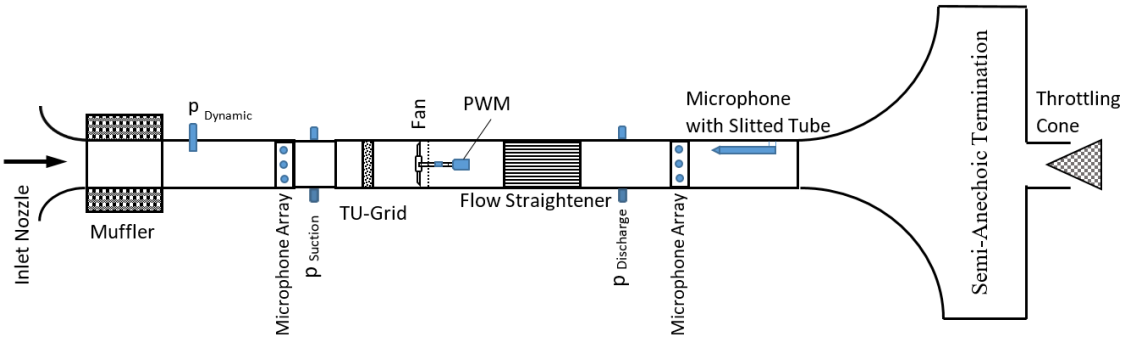

Fig. 2 Test rig according to DIN ISO 5136.

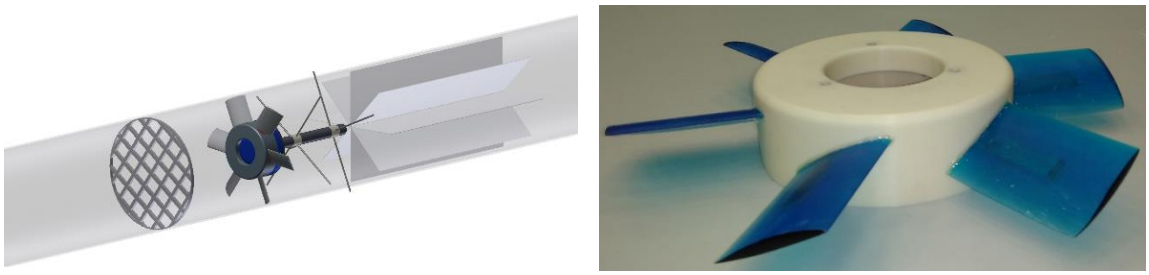

(a) Grid-Fan-Strut assembly (b) Prototype of investigated rotor

Fig. 3 Details of the test rig, more details are given in (Biedermann *et al.* 2018)

3.2 Measurement technique

On the suction and the discharge side of the fan, the rig is equipped with three ¼ -inch condenser microphones each, distributed equidistantly in the circumferential direction (Fig. 2). The microphones are used flush-mounted, where a side vented pressure field design allows for correct equalisation of the atmospheric pressure. Additionally, a ½ -inch condenser microphone with a slitted tube (turbulence screen) is mounted on the discharge side to gather aeroacoustic information for validation purposes. At a sampling rate of 44.1 kHz and a blocksize of 32768, spectral data of up to 17 kHz could be analysed at a frequency resolution $\Delta f = 1.3$ Hz. Applying Hanning windows with an overlap of 66%, the blocks are averaged 300 times, yielding a total measurement duration of 74 seconds. The rotor speed is monitored via a triaxial acceleration sensor ($\Delta f = 0.25$ Hz), mounted on the hub-support. In terms of aerodynamics, a pitot tube, located at the inlet nozzle, is used to measure the flow rate $\dot{Q}$ where the rise of static pressure Δp_{Fan} is obtained via two rings of pressure-tabbing points on the suction and the discharge side of the fan, resulting in a circumferentially averaged pressure of high accuracy. The power P_{Elec} of the pulse-width-modulated e-motor is obtained by use of a measuring calliper, leading to the systems' efficiency η_{System} (Eq. 1) of the fan. The aerodynamic data acquisition took place by applying a number of 20 averages.

$$\eta_{System} = \frac{\dot{Q} \cdot \Delta p_{Fan}}{P_{Elec}} \tag{1}$$

Table 1 Limits of the experimental space for the three analysed factors

Type	Unit	Min	Max
$\Delta z/D$	[--]	0.25	1.25
$\delta_{Throttle}$	[%]	0	100
n	[min^{-1}]	1000	2000

Table 2 Response variables of the analysed system

Classification	Aerodynamic			Aeroacoustics			Vibroacoustics
Type	Pressure	Flow rate	Efficiency	Pressure	Pressure	Pressure	Acceleration
Abbreviation	Δp_{Fan}	$\dot{Q}$	η_{System}	$p_{Suction}$	$p_{Discharge}$	p_{ST}	a_{Hub}
Unit	[Pa]	[m^3s^{-1}]	[%]	[Pa $_{RMS}$]	[Pa $_{RMS}$]	[Pa $_{RMS}$]	[ms^{-2}]

Upstream of the fan (Fig. 3), a biplane square grid (Fig. 3(a)) is used to generate elevated turbulent inflow level, where a ratio of five between grid bar diameter and mesh width proved to result in turbulence level of good isotropic character (Laws and Livesey 1978) at a sufficient distance from the grid. The distance between the grid and the rotor inside the duct is altered in order to generate continuously adjustable levels of incoming turbulence, which are analysed in more detail in
Section 4.

3.3 Test matrix and response variables

The chosen experimental space is of three dimensions, defined by the distance between grid and rotor $\Delta z/D$ (normalized by the fan diameter), the throttling state $\delta_{Throttle}$ and the fan speed n. The throttling state $\delta_{Throttle}$ defines the normalised flow rate of the system according to Eq. (2), independent of the fan speed, where 0% indicates an unrestricted system and vice versa.

$$\delta_{\mathrm{Throttle}} = 1 - \frac{\dot{Q}}{\dot{Q}_{\mathrm{Max.}}} \tag{2}$$

The variation of these parameters is expected to provide sufficient information on the systems' performance, that can be described by response variables still to be defined. For the statistical approaches by means of the Design of Experiments methodology, the influencing parameters need to be varied on three levels for the Box Behnken design and on five levels for the Central Composite design to satisfy the model complexity condition of order two. For the Latin Hypercube sampling, required for the Artificial Neural network, however, a number of variations in accordance with the amount of model data is needed. Despite the differences in the modelling approaches, the outer limits of each factor are fixed as Table 1 indicates. For the training of the chosen modelling approaches, however, the factor levels are all normalised in a range of Level = $\in$ (-1..1). The detailed run conditions for each sample are listed in Appendix A.

The definition of appropriate response variables turns out to be the crucial part of evaluating a given system as these variables are required to describe the systems characteristic performance with the necessary accuracy. Moreover, they need to be describable by means of the chosen influencing parameters. As it is already mentioned in Section 1, the response variables are of

aerodynamic and aeroacoustic/ vibroacoustic nature and are listed in Table 2. Aerodynamic parameters are the pressure rise Δp_{Fan} between suction and discharge side of the fan as well as the corresponding flow rate $\dot{Q}$. The systems' efficiency η_{System}, according to Eq. 1, defines the third response variable.

In terms of acoustics, the linear acoustic pressures of the suction side $p_{Suction}$ and the discharge side $p_{Discharge}$, including the acoustic signature of the slitted tube measurements p_{ST}, are decided to be implemented in the model. No sound pressure level is defined since the logarithmic scaling would distort the observed statistical effects. The acoustic pressure of both, the suction and discharge side is obtained by integrating the spectral energies in a bandpass of 100 Hz ≤ f ≤ 10 kHz, where the lower frequency is chosen due to limitations in the measurement environment. Vibroacoustic effects are incorporated in form of the acceleration a_{Hub} on the fan hub-support at frequencies of 0 Hz ≤ f ≤ 5 kHz.

4. Preliminary investigations

For further analysis and accurate modelling of the fan performance, it is essential that aerodynamic similarity laws are valid. With this purpose, the dimensional analysis helps to compare the fan performance at various operating conditions and to draw conclusions on the stability of the system within the covered experimental space. The non-dimensional pressure and flow values (Eq. (3)-(4)) lead to the elimination of the influence of the fan speed, reducing the throttling curves to a single curve as shown in Fig. 4a. On this basis, the percentage throttling state (Fig. 4(b)), independent of the fan speed, is defined using a function of 6th order, where a coefficient of determination of $R^2 = 0.9987$ is reached according to Eq. 5, where y_i is the observed response of the ith sample, $\hat{y}_i$ is the predicted response of the ith sample, $\bar{y}$ is the mean of the observed responses and n_{R^2} is the number of samples. This coefficient is a statistic used to describe the quality of an approximation by means of the variance, where $R^2 = 1$ indicates a perfect fit.

$$\psi = \frac{\Delta p_{Fan}/\rho}{U_0^2/2} \tag{3}$$

$$\phi = \frac{\dot{Q}}{U_0 \cdot A} \tag{4}$$

$$R^2 = 1 - \frac{\sum_i (y_i - \hat{y}_i)^2}{\sum_i (y_i - \bar{y})^2} \quad with \;\; i = 1..n_{R^2} \tag{5}$$

To obtain information on both, the local velocity distribution and the distribution of the grid-generated turbulence along the duct radius, 1-D hot wire measurements are conducted by use of a rotating channel, where the hot wire probe is traversed in the circumferential direction. Since no measurements are possible right in the rotor plane, a distance between grid and measurement plane is chosen, representing the distance to the later installed rotor but also neglecting possible distortion effects by the rotor in the upstream direction.

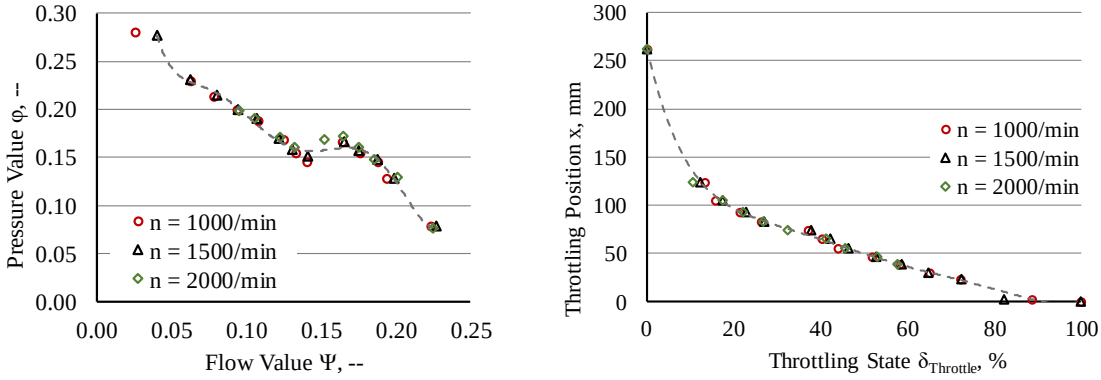

(a) Fan performance curve (b) Throttling curve

Fig. 4 Non-Dimensional fan characteristic curves at varying fan speed 1000 $min^{-1} \leq n \leq 2000\ min^{-1}$

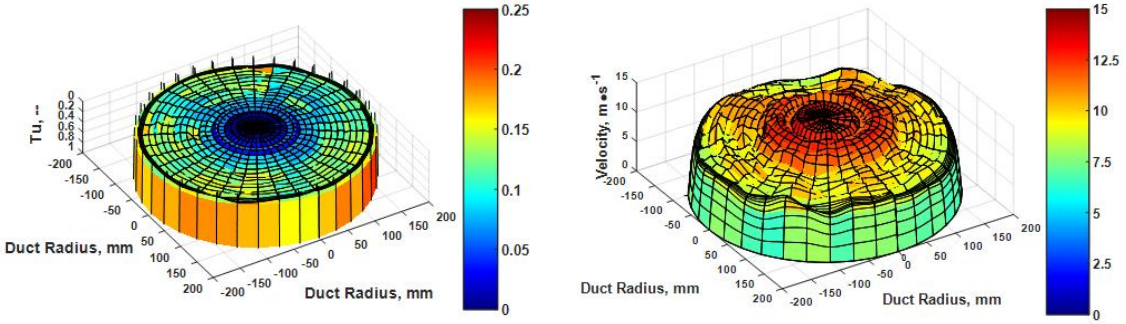

(a) Turbulence intensity Tu [--] (b) Longitudinal velocity U_0 [ms^{-1}]

Fig. 5 Profiles of turbulence intensity and axial velocity with turbulence grid at intermediate distance of $\Delta z/D = 0.75$ upstream the measurement plane, n = 2400 min^{-1}, $\dot{Q}/\dot{Q}_{Max} = 1$

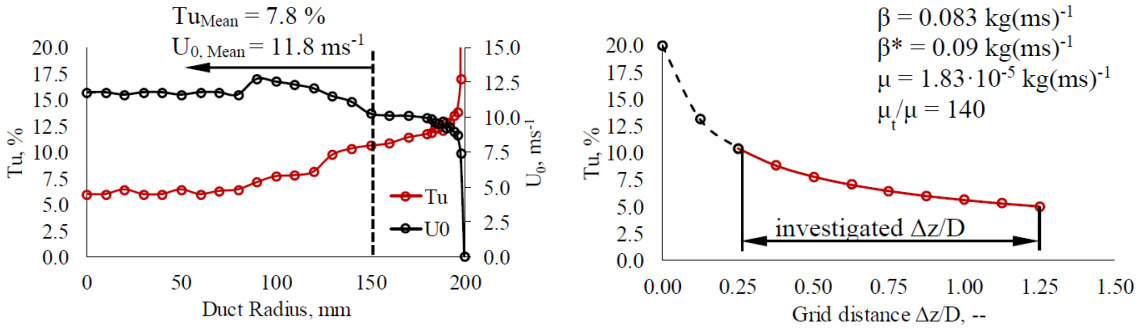

(a) Circumferentially averaged Tu and U_0 (b) Trend of the mean turbulence intensity as a function of the grid distance

Fig. 6 Averaged turbulence properties of the inflow

Fig. 5 shows the results with an increment of 10 deg or 53690 averaged samples per step, respectively. Turbulence intensity and velocity are inversely proportional, thus leading to low Tu level at high mean velocities and vice versa. Overall, the centre region ($R_{Duct} = \pm 0.1$ m) and the

outer region (-0.2 m ≤ R_{Duct} ≤ 0.2 m) of the duct show an adequate homogeneity in circumferential direction, where the radial trend shows a region of increased velocity (U_0 = 12.5 ms^{-1}) in the centre and reduced velocity (U_0 = 9 ms^{-1}) in the outer region. Averaging velocity and turbulence intensity over a radius of R_{Duct} = 0.15 m, to avoid the influence of the wall boundary layer, yields a mean velocity of $U_{0,\,Mean}$ = 11.8 ms^{-1} and a turbulence intensity of Tu_{Mean} = 7.8 % (Fig. 6a).

Increasing the grid distance to the rotor (Fig. 6b), however, leads to a continuous reduction of the turbulence intensity and thus also to a reduction of the primary noise source strength for the rotors' leading edges. Incorporating the average values of the previously reported hot wire measurements, the trend of the turbulence intensity right at the rotor leading edge is derived by an analytical model (ANSYS Inc. 2010) as a function of the grid location. Based on the initial turbulence intensity Tu_{ini}, the Tu at a given distance is determined according to Eq. (6), where ρ is the density of air, U_0 the free stream velocity, Δz/D the normalized grid distance, β and β* are model constants, μ is the dynamic fluid viscosity and μ_t the eddy viscosity. The results are shown in Fig. 6 (right) for the varied grid distance of 0.25 ≤ Δz/D ≤ 1.25.

$$Tu = \sqrt{\left({Tu_{ini}}^2 \left[1 + \frac{3 \cdot \rho \cdot U_0 \cdot \Delta z \cdot \beta \cdot Tu_{ini}^2}{2 \cdot \mu\left({}^{\mu_t}/_{\mu}\right)} \right]^{{}^{-\beta^*}/_{\beta}} \right)} \tag{6}$$

5. Results

5.1 Effect of parameters

Based on the trained Artificial Neural networks, various contour plots are generated, describing the influence of the analysed parameters on the response variables. Fig. 7 shows key-aerodynamic plots, whereas Fig. 8 shows trends on how single parameters affect the aeroacoustic response variables. The pressure rise of the fan clearly exhibits a dependency on both, fan speed n and throttling state $\delta_{Throttle}$, where maximum pressures are reached at maximum speed and throttling (Fig. 7(a)). In terms of the flow rate $\dot{Q}$ (Fig. 7(b)), the dominant parameter is the throttling state, only fractionally influenced by the fan speed. In contrast to the previously described trends of approximately quadratic nature, the systems' efficiency of the analysed fan is much more complex with a maximum at high speeds but low to intermediate throttling states and a minimum at low fan speed but high throttling states (Fig. 7(c)). The grid location, however, is not found to affect the pressure rise, the flow rate or the efficiency to high degrees.

Yet, moving the focus towards aeroacoustics (Fig. 8), the location of the turbulence grid does play an important role, especially at low throttling states or high flow rates, respectively. Small distances between grid and rotor lead to eddies of high energy (see also Fig. 6) impinging on the rotor leading edges and causing broadband leading edge noise. According to the energy cascade theory, larger grid distances lead, based on eddy dissipation effects, to decreasing turbulence intensities and thus to potential noise sources of lower energy. This pattern is confirmed by the contour plots for both, suction side noise (Fig. 8(a)) and discharge side noise (Fig. 8(b)), even though a local maximum occurs at maximum distances for the suction side, which might be caused by model uncertainties. At high throttling states, however, no (Fig. 8(a)) or only little (Fig. 8(b)) influences of the grid distances is visible.

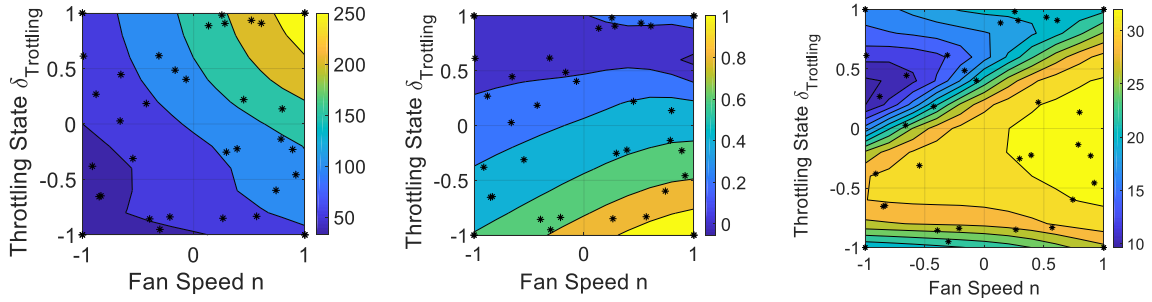

(a) Δp_{Fan} [Pa] (b) $\dot{Q}$ [m³s⁻¹] (c) η_{System} [%]

Fig. 7 Contour plots of aerodynamic response variables by varying normalised parameters. Contour shows results of Artificial Neural network, based on the LHS, where black stars indicate locations of the underlying measurement data pool

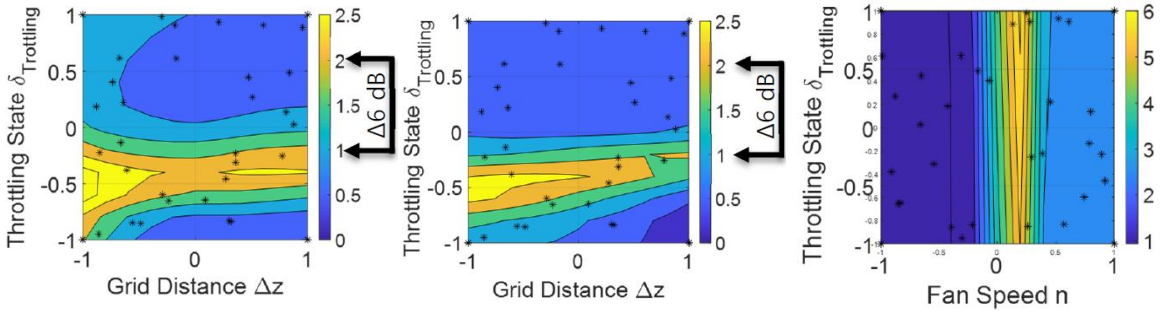

(a) $p_{Suction}$ [Pa RMS] (b) p_{Disch} [Pa RMS] (c) a_{Acc} [ms⁻²]

Fig. 8 Contour plots of aeroacoustic/ vibroacoustic response variables by varying normalised parameters. Contour shows results of Artificial Neural network, based on the LHS, where black stars indicate locations of the underlying measurement data pool

This is considered meaningful, since at high throttling states only low axial velocities are present, leading to a sharp decrease of the turbulence generated by the grid. During the measurement campaign, a clear tonal effect occurred at a fan speed of n = 1500 min^{-1} which is found to match the duct length resonance. Accordingly, as it is shown by the contour plot of the acceleration signal (Fig. 8(c)), a maximum in terms of acceleration is reached at the fan hub-support, turning out to be independent of the throttling state.

5.2 Comparison of models

Three experimental designs are adopted and applied to a given system with the aim to describe it with the highest possible accuracy while varying three parameters of interest. The Box Behnken design and the Central Composite design are used to define a model of second order, while Latin Hypercube sampling is used for the training of an Artificial Neural network. All generated models are rated by the coefficient of determination R^2, which is determined according to Eq. 5. The coefficient of determination allows assessing how well the observed values of a systems' response can be approximated by the output of a model. A value close to one means that the unexplained variance of the model is relatively small compared to the total variance of the data, thus representing a good approximation.

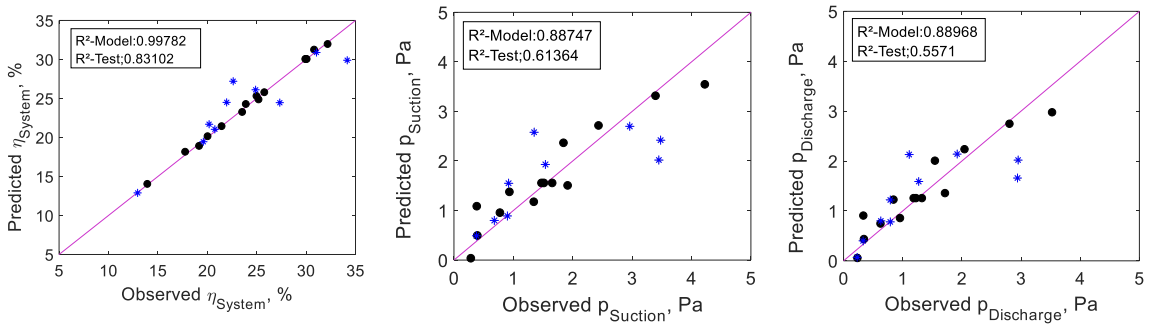

(a) $p_{Suction}$ [Pa RMS] (b) p_{Disch} [Pa RMS] (c) $p_{Disch.}$ [Pa RMS]

Fig. 9 Box-Behnken design: Observation/ prediction plots for different target values, indicating the fit of the employed models. Blue stars indicate model-independent test data, black circles indicate data used to model the response surface regression

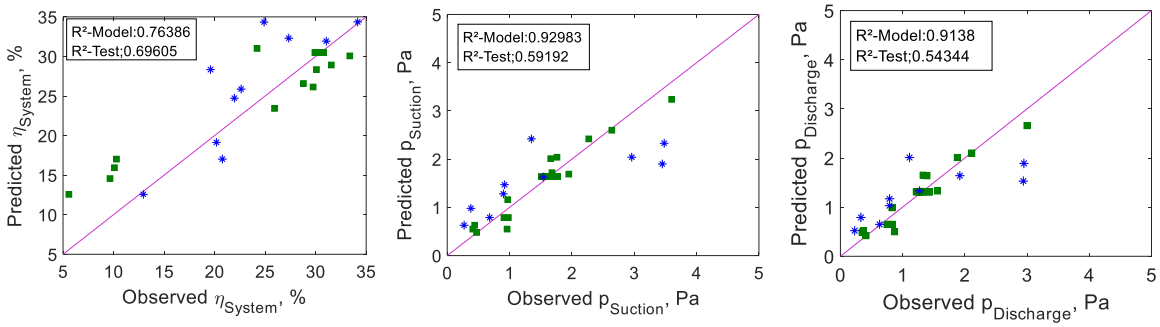

(a) η_{System} [%] (b) $p_{Suction}$ [Pa RMS] (c) $p_{Disch.}$ [Pa RMS]

Fig. 10 Central Composite design: Observation/ prediction plots, indicating the fit of the employed models. Blue stars indicate model-independent test data, green rectangles indicate data used to model the response surface regression

Figs. 9-11 show the observation/ prediction-plots for the most challenging response variables, namely the systems' efficiency as well as the acoustic noise radiation on the suction and on the discharge side of the fan.

It is seen that the fit of the model itself shows high values for all chosen approaches, albeit the Box-Behnken design's response surface regression (Fig. 9) shows the highest values for the systems' efficiency and the Artificial Neural network, based on the Latin Hypercube sampling (Fig. 11) fits best for the acoustic response variables. Analysing the fit of the test data, however, shows a dramatic decrease of the performance for the quadratic models but high performance for the Artificial Neural network, even though there is still space to further improve it. The performance for all response variables and approaches is summarised in Table 3. As it is already indicated by the contour plots in Figs. 7 and 8, the aerodynamic trends of Δp_{Fan} and $\dot{Q}$ are properly describable by a quadratic model, what matches the fluid mechanics' theory. On the contrary, the mapping of the systems' efficiency tends to be more challenging and even collapsing when it comes to aeroacoustics, requiring a more complex modelling approach. Despite that the experimental effort of the LHS increases by 17% (24 → 28 runs) for the C-CCD or 87% for the BBD (15 → 28 runs), respectively, the performance in form of the coefficient of determination R^2 with regard to the test data for $p_{Suction}$ increases by 65% (79% $p_{Discharge}$) compared to the C-CCD approach and 59% (75% $p_{Discharge}$) compared to the BBD approach.

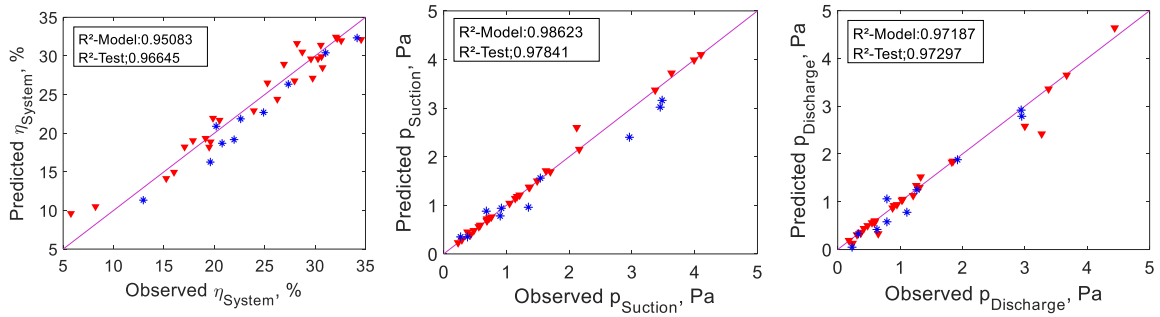

(a) η_{System} [%] (b) $p_{Suction}$ [Pa RMS] (c) $p_{Disch.}$ [Pa RMS]

Fig. 11 Latin Hypercube sampling: Observation/ prediction plots, indicating the fit of the employed models. Blue stars indicate model-independent test data, red triangles indicate data used to model the response surface regression

Table 3 Coefficients of determination R^2 for model data and independent test data, comparing different approaches

		No. Samples	Δp_{Fan}	$\dot{Q}$	η_{System}	$p_{Suction}$	$p_{Discharge}$	p_{ST}	a_{Hub}
BBD	Model Data	15	0.999	0.995	0.998	0.887	0.889	0.879	1.000
	Test Data	10	0.993	0.991	0.831	0.614	0.555	0.555	0.648
CCD	Model Data	24	0.973	0.957	0.727	0.934	0.918	0.930	0.614
	Test Data	10	0.969	0.937	0.696	0.593	0.543	0.507	0.504
LHS	Model Data	28	0.997	0.997	0.951	0.986	0.972	0.967	0.974
	Test Data	10	0.995	0.994	0.966	0.978	0.973	0.975	0.947

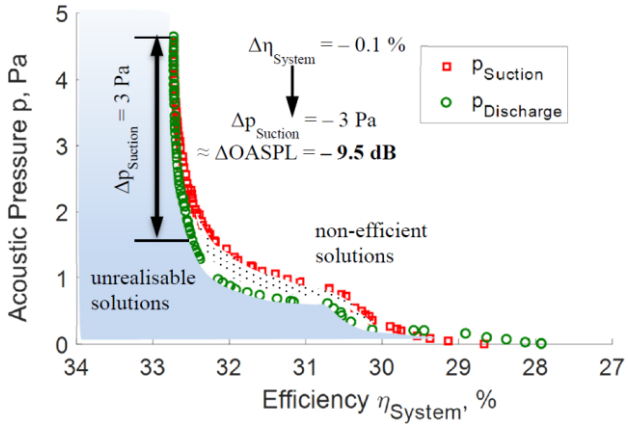

Fig. 12 Pareto optimal solutions (Pareto front). Minimising the acoustic pressure while maximising the systems' efficiency η_{System}

5.3 Multi-objective optimisation

It is often the case that two or more objectives are conflicting. This is especially true for aeroacoustics, where the dilemma of opposing trends in terms of aerodynamics and aeroacoustics

is a common challenge. This means that the ideal solution for one objective can lead to a disadvantageous solution for another objective. Computational expensive unbiased multi-objective optimisation is able to compute Pareto optimal solutions, visualised by the so-called Pareto front, which separates non-efficient from unrealizable solutions. The Pareto front also helps to indicate solutions that may be of beneficial character compared to others. Using ANNs with good accuracy to approximate the Pareto front is a powerful and fast way of optimising the underlying system. Fig. 12 shows the Pareto front for the optimum of the systems' efficiency η_{System} and the acoustic radiation on the suction $p_{Suction}$ and discharge $p_{Discharge}$ side, where minimum acoustic pressures are desired while keeping the efficiency on high values. Figure 12 indicates that e.g. a small reduction in efficiency of $\Delta\eta_{System} = 0.1$ % ($\eta_{System} \approx 32.5\% \rightarrow \eta_{System} \approx 32.4\%$) can lead to a tremendous reduction in acoustic radiation of $\Delta OASPL \approx 9.5$ dB ($p_{Discharge} \approx 4.5$ Pa $\rightarrow p_{Discharge} \approx 1.5$ Pa) on the discharge side of the fan.

Physically speaking, the condition of maximum efficiency is reached at the highest fan speed ($n = +1$) and at an intermediate throttling state ($-0.5 \leq \delta_{Throttle} \leq 0.1$). The grid position $\Delta z/D$, however, does only play a minor role. Acoustically, reaching optimum flow conditions at $\delta_{Throttle} \approx -0.5$, including blade congruent inflow for the rotor blades, a minimum of noise is radiated at high aerodynamic efficiency. With further throttling $\delta_{Throttle} > -0.5$, however, a gradual stall is induced for the blade tip region on the suction sides of single blades, which does not yet affect the global aerodynamic efficiency. On the contrary, even a slight increase in efficiency is observed since a higher static pressure rise is generated. But, in contrast to the aerodynamic performance, the regions with separated flow do represent noise sources of significant strength, resulting in a sharp increase of the radiated noise. In result, it is arguable whether the fan is already operating at (aerodynamic) on or off-design conditions since for the specifically tested rotor the design condition is very close to the instability region. Nonetheless, in either case, the Pareto front helps to indicate such unfortunate operating conditions by providing multi-objective information on both, aerodynamic efficiency and noise radiation.

6. Spectral application

As it is shown in the previous section, the use of Artificial Neural networks (combined with LHS) allows for a precise and accurate prediction of all the target values as well as a good approximation of the investigated experimental space. However, especially in aeroacoustics and vibroacoustics, information on the spectral shape is of essential value for providing additional information on the underlying noise generation mechanisms of e.g., fans. Moreover, accounting for the human perception of noise by means of the relative loudness (e.g., A-weighting) requires a frequency analysis as well, since it takes place solely in the frequency domain.

Therefore, the drawn conclusions on the superiority of the ANNs vs. the classic modelling approaches are directly adopted for the purpose of processing the already available experimental data towards a spectral model. For this case study, a training algorithm according to Bayesian learning (Dan Foresee and Hagan 1997) is used since no splitting into training and validation data is needed. Due to the fact that only ANNs are regarded and all gained information shall be used, the full experimental data basis, including data points from the LHS, the C-CCD, the BBD as well as data points from the test design (excluding one for actually testing), can be used for a proof-of-concept with regard to spectral approximation. The resulting ANNs do not directly provide information of the systematic relation and influence of parameters on the target values. However,

performing parametric studies based on the ANNs by varying single influencing parameters solves this dilemma and offers similar benefits than the models based on the Design of Experiments methodology.

In order to maximise the spectral information while keeping the amount of data on a reasonable level, 1/3rd octave band in a mid-frequency range of 16 Hz ≤ f ≤ 10 kHz are analysed. This results, in addition to the already described target values, in 58 extra target values, each one representing a fully independent ANN, describing the sound pressure of just one 1/3rd octave band.

6.1 Model fit

The training of the ANNs is performed by use of the complete measurement data pool but for one data point, which is used for independent testing. During the training with the above-mentioned algorithm, the maximum relative deviation is used to evaluate different networks. The performance is measured by using the training data and calculating the relative deviation in comparison to the observation of every approximated 1/3rd octave band for every data point. Table 4 shows the maximum, the mean as well as the median of the deviations, in both, the decibel-scale and the (linear) Pascal-scale, separated for the suction side and the discharge side. Especially in the field of aeroacoustics, it is important to note that solely the uncertainty related to the Pascal-scale shows a physically interpretable fit of the model, while the dB-scale is more related to the human perception of sound. Thus, the deviation in the dB-scale highly depends on the referenced underlying mean level since it scales logarithmically.

For the analysed data, the median and the mean deviation show a reasonably good fit of the model with variations smaller than 5% in the Pa-scale where the discharge side outperforms the suction side. This is assigned to a slightly better aeroacoustic treatment of the discharge side by the anechoic ending, showing an improved ability to suppress back reflections at the duct exit due to impedance differences. The maximum deviation, though, is significantly higher and indicates the need for further validation and a possibly increased data pool to decrease the experimental noise. For gaining a slight insight into the ability to generalise, one independent data point, that is not part of the training data, is used for a prediction of the spectral information. The comparison between the prediction and the gathered experimental data is presented in Fig. 13 for the suction side (Fig. 13a) and the discharge side (Fig. 13b). Qualitatively, the trend of the SPL with the frequency is considered to be well-approximated. The same applies to the quantitative nature of the prediction, even though single frequencies exhibit a lack of fit, affecting the total accuracy of the modelled experimental space.

Table 4 Averaged fit of 29 1/3rd octave bands at mid-frequencies 16 Hz ≤ f ≤ 10 kHz

	Suction Side		Discharge Side	
	dB–scale	Pa–scale	dB–scale	Pa–scale
Median Deviation in %	0.30	2.70	0.26	2.25
Mean Deviation in %	0.53	4.93	0.46	4.15
Maximum Deviation in %	4.58	46.12	6.21	65.01

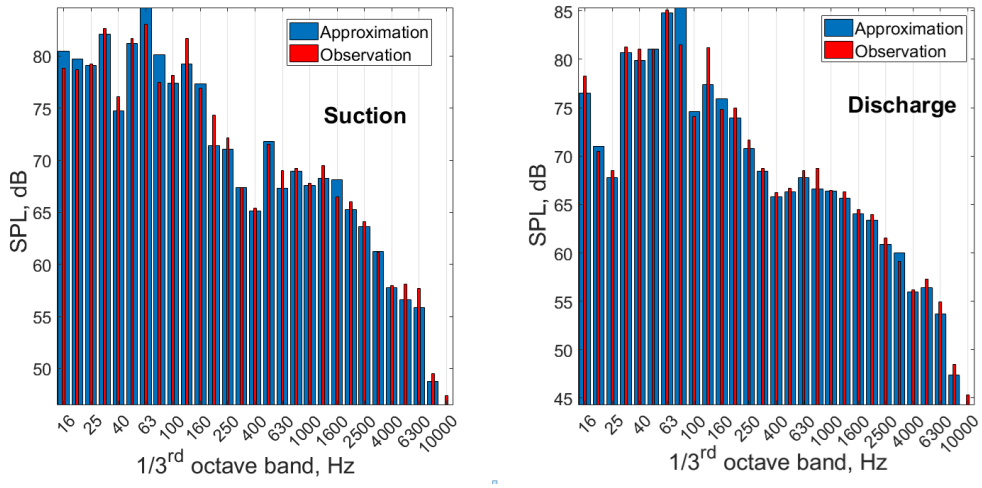

(a) Predicted/ observed suction side noise (b) Predicted/ observed discharge side noise

Fig. 13 Spectral content by means of 1/3rd octave bands. Comparison to independent test data at Δz/D = 1.005, n = 1061 min^{-1}, δ = 63.4%

6.2 Parametric study

One of the main benefits having developed a spectral model is the possibility to obtain structured information on the effect of single influencing parameters with regard to the noise radiation at the different analysed 1/3rd octave bands. Fig. 14 shows a continuous variation of the factor level in 30 equidistant steps for all three investigated factors. The wavy shape of the low-to-intermediate frequency region for all the shown plots is linked to the presence of tonal effects at the fundamental frequency and at the integer multiples or harmonics, respectively. Increasing the rotational speed (Fig. 14a) shows a predominant effect of increasing intermediate-frequency noise, which becomes more and more significant for the overall sound pressure level. Meanwhile, at low frequencies, still a noise increase takes place but of attenuated effect.

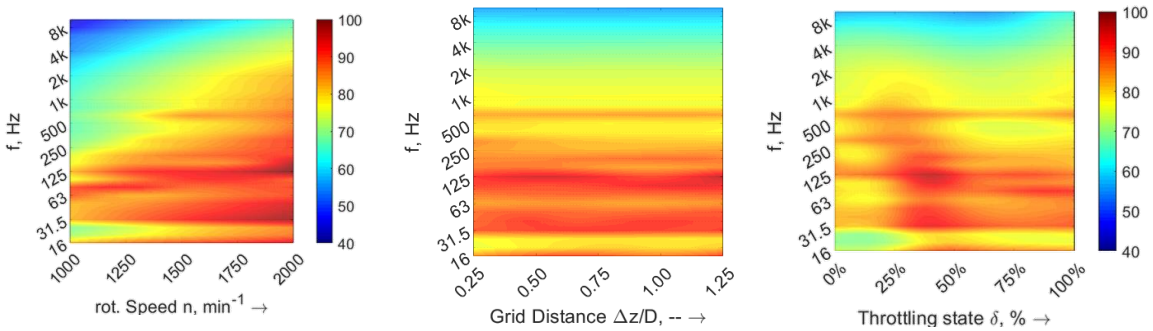

(a) Rotational speed (b) Grid distance (c) Throttling state

Fig. 14 Spectral sound pressure level (discharge side), showing the main effects of the analysed parameters. Variation of one parameter in 30 equidistant steps while the other parameters remain on an intermediate level

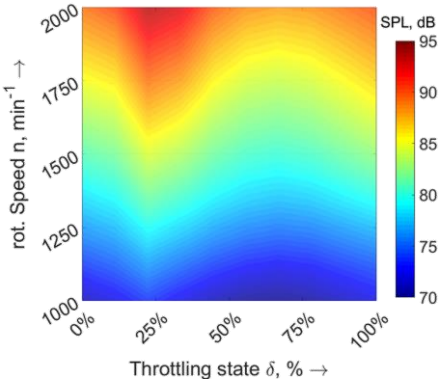

Fig. 15 Interdependent effect of rotational speed and throttling state on the noise radiation within the 1 kHz octave band (averaged 800 Hz, 1000 Hz and 1250Hz 1/3rd octave bands)

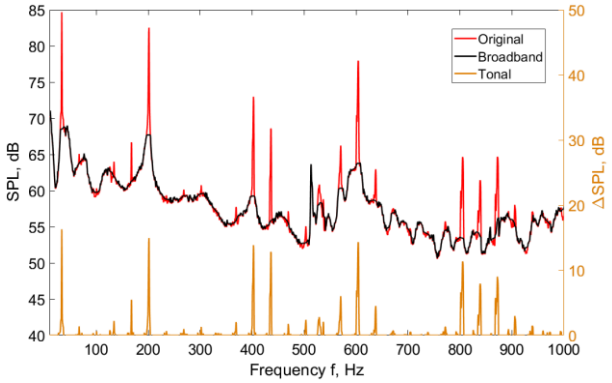

Fig. 16 Exemplarily filtered measurement result using a first order median filter of 30 samples. Filtered broadband signal (black) and extracted speed-dependent tonal components (orange)

This staircase-shaped pattern from low to high frequencies is due to a speed-dependent shift of the tonal components which scale with the fundamental frequency. High frequencies show only little increase of the radiated level. Varying the grid distance (Fig. 14(b)) shows no effect comparable in significance to the influence of the rotational speed or the throttling state. Nevertheless, the results are still considered meaningful, since the influence of $\Delta z/D$ only becomes significant at sufficiently high mean velocities as it is the case for low throttling states $\delta_{Throttle} \leq 0$ (also confirmed by trends in Fig. 8(a)-8(b)). The isolated effect of the throttling state in Fig. 14c shows significant noise radiation in the low-to-intermediate frequency region. Increasing the throttling state from 0% to 100% or decreasing the flow rate from maximum towards zero, respectively, shows a strong increase of the radiated noise at $\delta_{Throttle} \approx 25\%$, indicating the aerodynamic instability region, where flow separation occurs (see Fig. 4(a)). At $\delta_{Throttle} \approx 50\%$, the fan performs on a secondary characteristic, leading to a local reduction of the SPL before large scale separation occurs at throttling states $\delta_{Throttle} \geq 75\%$ and low-frequency noise become dominant.

With respect to the human perception of noise, the 1 kHz octave band, which is the only octave band not affected by any weighting functions, is extracted from the three associated 1/3rd octave bands according to Eq. (7), covering a frequency range of $710\ Hz \leq f \leq 1420\ Hz$. This limitation to

a single frequency band enables to investigate the interdependent effect of throttling state and rotational speed on the noise radiation as shown in Fig. 15.

$$SPL_{Oct,1kHz} = 10\lg\left(10^{SPL_{800Hz}/10} + 10^{SPL_{1000Hz}/10} + 10^{SPL_{1250Hz}/10}\right) \quad (7)$$

As discussed before, the noise radiation increases with the rotational speed where Fig. 15 shows an amplified effect at higher speeds as more dominant harmonics of the blade passing frequency tend to affect the 1 kHz octave band. With regard to the throttling state, no strong change in the radiated pattern as a function of the rotational speed is observed, indicating only weak interdependencies between the two analysed parameters. Nevertheless, a distinct effect of the throttling state on the SPL is present, following the aerodynamic fan curve with increased noise radiation in the instability region ($25\% \leq \delta_{Throttle} \leq 50\%$) and reduced radiation at primary and secondary characteristics $\delta_{Throttle} \leq 25\%$ or $\delta_{Throttle} \geq 50\%$, respectively.

6.3 Discussion

One of the main benefits but also one of the main restrictions of the chosen modelling approach is the independent nature of the ANNs for each 1/3rd octave band that hinders a cross-transfer of spectral information. Thus, slight variations such as for example in the rotational speed might lead to a shift of the tonal components or the BPF from one 1/3rd octave band into the neighbouring one, leading to a strong increase of the complexity of the experimental space and/ or the requirements for the modelling approach. These effects are also suspected to be a significant contributor to the observed (in)accuracy of the presented spectral model (see *Section 6.1*). Aiming at enabling a more coherent modelling of the aeroacoustic fan characteristics, an alternative approach might be to extend the current approach by an additional separation of the tonal from the broadband components of the underlying spectra. This can be achieved by the use of median filtering of the experimental data basis as shown exemplarily for one measurement point in Fig. 16, where the spectral content is separated in broadband and tonal portions. In this regard, the broadband components of each frequency band can still be modelled independently but avoiding the disturbing effects of shifting significant tonal components between the single octave bands or the influence of possibly occurring duct modes. The separately modelled speed-dependent tonal fraction is added at a later stage.

7. Conclusions

Detailed experiments are conducted to analyse the aerodynamic and aeroacoustic performance of an axial fan as a benchmark case. Three different approaches are analysed in terms of required experimental effort and modelling accuracy. The circumscribed Central Composite design (C-CCD) and the Box Behnken design (BBD) approaches are limited to models of second order whereas for the Latin Hypercube sampling (LHS), in combination with an Artificial Neural network, no such restriction in model complexity is predetermined. The results obtained allow the current paper to reach the following conclusions:

The Latin Hypercube sampling in combination with an Artificial Neural network yields, based on the test data, improved average performance of 44% compared to the Central Composite design and 32% compared to the Box-Behnken design. Especially the system efficiency η_{System} and the aeroacoustic/ vibroacoustic parameters ($p_{Suction}$, $p_{Discharge}$, a_{Hub}) turned out to be highly non-linear,

hence preventing an acceptable approximation accuracy by the classic BBD or C-CCD approaches. The obtained results by the ANNs reproduce the trends of the individually tested parameters with high quality. Even validated against independent test data at extreme parameter settings, which are naturally hard to approximate, the LHD shows a good performance. On the other hand, the good approximation quality comes at the cost of an increased number of model samples for the LHS which is +17% for the C-CCD and +87% for the BBD, respectively.

Subsequent processing of the obtained ANNs towards an unbiased multi-objective optimisation in form of Pareto optimal solutions uncovered disadvantageous parameter combinations for the aerodynamic efficiency and the associated noise radiation. At comparable aerodynamic efficiency ($\Delta\eta_{System}$ = 0.1%), remarkable differences in the radiated overall noise level are predicted (ΔOASPL = 9.5 dB), being in line with the underlying physical mechanisms. The multi-objective analysis of several target values is considered to be a helpful tool for future low-noise design purposes.

Encouraged by the high accuracy of the generated approximation model, the ANNs are further developed by implementing spectral information on the aeroacoustic performance. The approximated 1/3rd octave band spectra show a reasonably good fit, being impaired by influences of supposedly shifting tonal components and high experimental noise, corrupting the accuracy. With the implemented spectral composition not only the overall sound pressure level is predictable for each parameter combination within the bounds of the experimental space, but also accounting for the human perception of noise (A-weighting in the frequency domain) becomes possible.

Eventually, inspired by the underlying physical noise generation mechanisms, a modification of the used approach is suggested in form of an isolated prediction of the tonal and the broadband components for each 1/3rd octave band. This is considered meaningful to further improve the spectral prediction accuracy for the ANNs.

Acknowledgments

The authors gratefully acknowledge the kind support of M.Sc. students Nils Hintzen and Matthias Rother as well as B.Eng. student Nina Balde in setting up the test rig and conducting the experiments.

References

Adam, M. (2012), “Statistische Versuchsplanung und Auswertung (DoE Design of Experiments)”, Lecture Notes, University of Applied Sciences Dusseldorf, Germany.

Alam, F.M., McNaught, K.R. and Ringrose, T.J. (2004), “A comparison of experimental designs in the development of a neural network simulation metamodel”, *Simul. Modell. Practice Theor.*, **12** (7-8), 559-578. https://doi.org/10.1016/j.simpat.2003.10.006.

Amiet, R K. (1977), “Noise produced by turbulent flow into a propeller or helicopter rotor”, *AIAA J.*, **15**(3), 307-308. https://doi.org/10.2514/3.63237.

ANSYS Inc. (2010), *ANSYS CFX-Solver Theory Guide*, Release 12.1, ANSYS Inc., Southpointe, U.S.A.

Biedermann, T.M., Chong, T.P., Kameier, F. and Paschereit, C.O. (2017), “Statistical-empirical modelling of airfoil noise subjected to leading edge serrations”, *AIAA J.*, **55**(9), 3128-3142. https://doi.org/10.2514/1.J055633.

Biedermann, T.M., Kameier, F. and Paschereit, C.O. (2018), “Optimised test rig for measurement of aerodynamic and aeroacoustic performance of leadingedge serrations in low-speed fan application”,

Proceedings of the ASME Turbo Expo 2018, Oslo, Norway, June.
Box, G.E. and Behnken, D.W. (1960), "Some new three level designs for the study of quantitative variables", *Technometrics*, **2** (4), 455-475. https://doi.org/10.2307/1266454.
Carolus, T.H. and Starzmann, R. (2011), "An aerodynamic design methodology for low pressure axial fans with integrated airfoil polar prediction", *Proceedings of the ASME Turbo Expo 2011*, Vancouver, Canada, June.
Daroukh, M., Moreau, S., Gourdain, N., Boussuge, J.F. and Sensiau, C. (2017), "Influence of distortion on fan tonal noise", *Proceedings of the 22nd AIAA/CEAS Aeroacoustic Conference*, Lyon, France, June.
Foresee, F.D. and Hagan, M.T. (1997), "Gauss-newton approximation to bayesian learning", *Proceedings of the International Conference on Neural Networks (ICNN'97)*, Houston, U.S.A., June.
ISO 5136 (2009), *DIN EN ISO 5136:2009-11*, Acoustics – Determination of sound power radiated into a duct by fans and other air moving devices – In-duct method (ISO 5136:2003), Deutsches Institut für Normung e.V., Berlin, Germany. https://dx.doi.org/10.31030/1545135.
Joseph, V.R. and Hung, Y. (2008), "Orthogonal-maximin Latin hypercube designs", Statistica Sinica, **18**(1), 171-186. https://jstor.org/stable/24308251.
Laws, E.M. and Livesey, J.L. (1978), "Flow through screens", *Annu. Rev. Fluid Mech.*, **10**(1), 247-266. https://doi.org/10.1146/annurev.fl.10.010178.001335.
McKay, M.D., Beckman, R.J. and Conover, W.J. (1979), "A comparison of three methods for selecting values of input variables in the analysis of output from a computer code", *Technometrics*, **42**(1), 55-61. http://jstor.org/stable/1271432.
NIST/SEMATECH (2003), *e-Handbook of Statistical Methods*, U.S. Department of Commerce, Gaithersburg, U.S.A.
Reich, M., Adam, M. and Lambach, S. (2017), "Comparison of different methods for approximating models of energy supply systems and polyoptimising the systems-structure and components-dimension", *Proceedings of the ECOS 2017 - The 30th International Conference on Efficiency, Cost, Optimization and Environmental Impact of Energy Systems*, San Diego, California, U.S.A., July.
Samarasinghe, S. (2007), *Neural Networks for Applied Sciences and Engineering: From Fundamentals to Complex Pattern Recognition*, Auerbach Publications, Boca Raton, Florida, U.S.A.
Siebertz, K. van Bebber, D. and Hochkirchen, T. (2010), *Statistische Versuchsplanung*, Springer Company, Berlin, Germany.
Viana, F.A. (2013), "Things you wanted to know about the latin hypercube design and were afraid to ask", *Proceedings of the 10th World Congress on Structural and Multidisciplinary Optimization*, Orlando, Florida, U.S.A., May.
Zenger, F., Herold, G. and Becker, S. (2016), "Acoustic characterization of forward- and backward skewed axial fans under increased inflow turbulence", *Proceedings of the 22nd AIAA/CEAS Aeroacoustics Conference*, Lyon, France, June.

CC

Nomenclature

DoE	Design of Experiments
ANN	Artificial Neural network
C-CCD	Circumscribed Central Composite design
BBD	Box Behnken design

LHS	Latin Hypercube sampling
BPF	blade passing frequency
A	rotor area [m^2]
a_{Hub}	acceleration [$m \cdot s^{-2}$]
C	blade chord [mm]
D	rotor diameter [mm]
n	fan speed [s^{-1}]
n_{R^2}	number of samples [--]
P_{Elec}	electric power [W]
p_{ST}	acoustic pressure of slitted tube [Pa $_{RMS}$]
$p_{Suction}$	acoustic pressure at suction side [Pa $_{RMS}$]
$p_{Discharge}$	acoustic pressure at discharge side [Pa $_{RMS}$]
$\dot{Q}$	flow rate [$m^3 \cdot s^{-1}$]
R_{Duct}	duct radius [mm]
R^2	Coefficient of determination [--]
S	blade span [mm]
SPL	(local) Sound Pressure Level [dB]
Tu	turbulence intensity [--]
U	circumferential velocity [$m \cdot s^{-1}$]
U_0	free stream velocity [$m \cdot s^{-1}$]
x	throttling position [m]
y_i	observed response value [diverse]
$\hat{y}_i$	predicted response value [diverse]
$\bar{y}$	mean of observed response [diverse]
β, β*	model constants [$kg \cdot (ms)^{-1}$]

$\delta_{Throttle}$ throttling state [--]

Δf frequency resolution [Hz]

$\Delta OASPL$ Overall Sound Pressure Level [dB]

Δp static pressure rise [Pa]

$\Delta z/D$ grid distance [--]

η_{System} system efficiency [--]

μ fluid viscosity [$kg \cdot (ms)^{-1}$]

μ_t eddy viscosity [$kg \cdot (ms)^{-1}$]

μ_t/μ eddy viscosity ratio [--]

ρ air density [$kg \cdot m^{-3}$]

φ flow value [--]

ψ pressure value [--]

Appendix A

Table 5 Experimental run conditions for the individual tested statistical approaches, normalized by the parameter limits of grid distance Δz/D, fan speed n and throttling state $\delta_{Throttle}$

	Latin Hypercube			**Central Composite**			**Box Behnken**			**Test Data**		
No.	**Δz/D**	**n**	**$\delta_{Throttle}$**	**Δz/D**	**n**	**$\delta_{Throttle}$**	**Δz/D**	**n**	**$\delta_{Throttle}$**	**Δz/D**	**n**	**$\delta_{Throttle}$**
1	1.00	-1.00	-1.00	-1.00	-1.00	-1.00	-1.00	-1.00	0.00	-1.00	-1.00	-1.00
2	-1.00	1.00	-1.00	-1.00	-1.00	1.00	-1.00	1.00	0.00	1.00	1.00	-1.00
3	-1.00	-1.00	1.00	-1.00	1.00	-1.00	1.00	-1.00	0.00	1.00	-1.00	1.00
4	1.00	1.00	1.00	-1.00	1.00	1.00	1.00	1.00	0.00	-1.00	1.00	1.00
5	0.47	-0.65	0.45	1.00	-1.00	-1.00	-1.00	0.00	-1.00	-0.48	-0.40	-0.86
6	0.32	-0.21	-0.84	1.00	-1.00	1.00	-1.00	0.00	1.00	0.77	0.29	-0.25
7	-0.30	0.25	0.98	1.00	1.00	-1.00	1.00	0.00	-1.00	0.21	0.52	0.93
8	-0.61	-0.91	-0.38	1.00	1.00	1.00	1.00	0.00	1.00	-0.29	0.74	-0.60
9	0.81	0.80	0.14	-1.68	0.00	0.00	0.00	-1.00	-1.00	-0.73	-0.07	0.40
10	-0.85	0.39	-0.22	1.68	0.00	0.00	0.00	-1.00	1.00	0.51	-0.88	0.27
11	0.36	-0.55	-0.31	0.00	-1.68	0.00	0.00	1.00	-1.00			
12	0.95	0.13	0.89	0.00	1.68	0.00	0.00	1.00	1.00			
13	-0.17	-0.99	0.61	0.00	0.00	-1.67	0.00	0.00	0.00			
14	0.27	0.92	-0.46	0.00	0.00	1.67	0.00	0.00	0.00			
15	-0.86	-0.30	-0.95	0.00	0.00	0.00	0.00	0.00	0.00			
16	-0.64	0.45	0.22	0.00	0.00	0.00						
17	-0.67	-0.31	0.62	0.00	0.00	0.00						
18	-0.66	0.79	-0.14	0.00	0.00	0.00						
19	0.30	0.57	-0.83	0.00	0.00	0.00						
20	-0.24	-0.85	-0.65	0.00	0.00	0.00						
21	0.60	0.28	0.91	0.00	0.00	0.00						
22	0.88	-0.66	0.03	0.00	0.00	0.00						
23	0.84	-0.17	0.49	0.00	0.00	0.00						
24	0.36	0.89	-0.23	0.00	0.00	0.00						
25	-0.56	0.26	-0.85									
26	-0.18	0.61	0.91									
27	-0.88	-0.43	0.18									
28	0.09	-0.83	-0.65									